Oil & Natural Gas Technology

DOE Award No.: DE-FE0009904

Quarterly Research Performance Progress Report (Period ending 3/31/2015)

Structural and Stratigraphic Controls on Methane Hydrate occurrence and distribution: Gulf of Mexico, Walker Ridge 313 and Green Canyon 955

Project Period: 10/01/2012 – 09/30/2015

Submitted by:

Priyank Jaiswal

Signature

Office of Fossil Energy

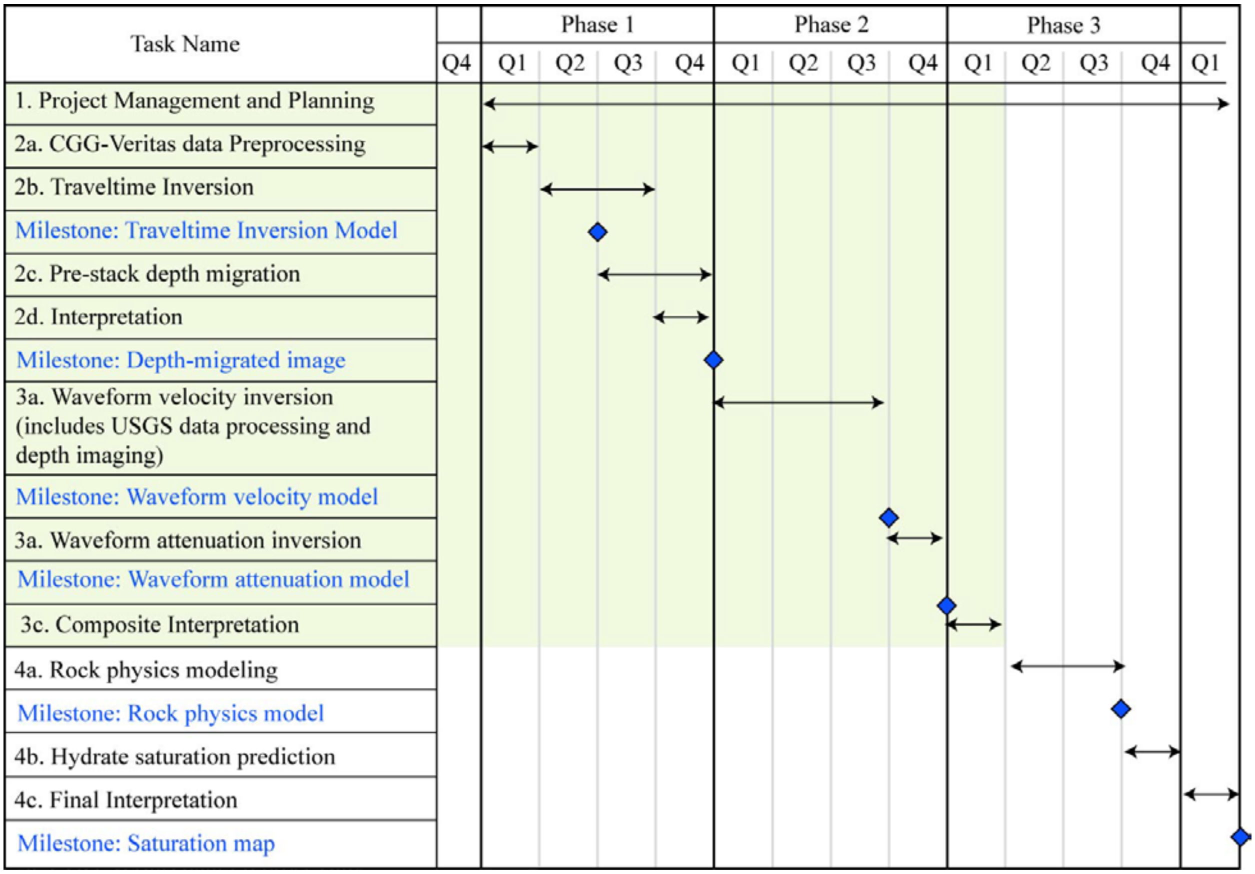

Table 1. Gantt chart. The project is on target till date. Tasks already completed in the milestone chart are shaded in green.

Executive Summary

This quarterly progress summarizes the progress made towards completion of Phase 2, Subtask 3c which comprises composite interpretation of Full Waveform Inversion (FWI) and depth migrated image.

Background

The overall objective is to identify and understand structural and stratigraphic controls on hydrate accumulation and distribution in leased blocks WR313 (WR: Walker Ridge) and GC955 (GC: Green Canyon) in the Gulf of Mexico using seismic and well data (Figure 1). The effort is to be completed in three phases. In the first phase, the objective is to create a large-sale (resolution in the order of Fresnel zone) P-wave velocity model using traveltime inversion and a corresponding depth image using pre-stack depth migration (PSDM). This phase was completed in due time.

At the end of the second phase, which is the topic of this report, the objective was to jointly interpret the pre-stack depth migrated images and the full-waveform V_P models that from Phase 1 and Phase 2 deliverables. This phase is also on target.

The third phase has two objectives. The first objective is to create a hydrate distribution map with the help of P-wave velocity and attenuation model created in the second phase and standard rock physics modeling method. The second objective is to jointly interpret all available datasets to determine the structural and stratigraphic controls on hydrate occurrence and distribution.

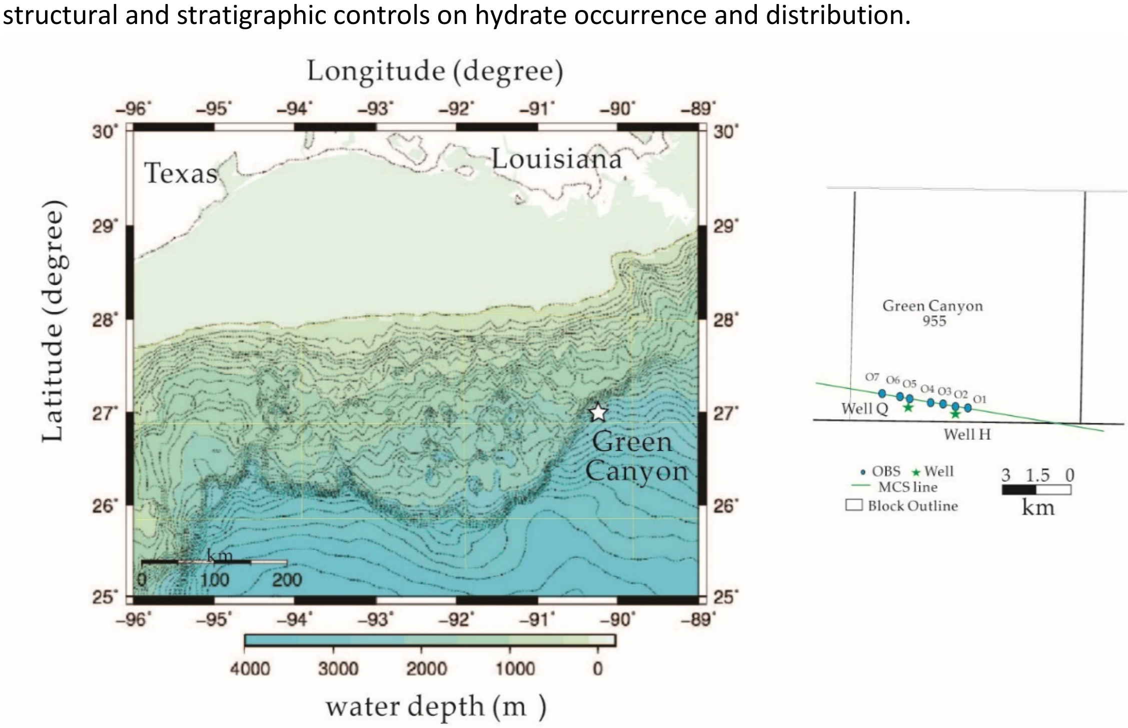

Figure 1: Base map. Seafloor bathymetry of Gulf of Mexico showing the location of the study area at the mouth of Green Canyon. The acquisition layout within lease block Green Canyon 955 (GC955) is shown in the inset. Solid line is the track of the multi-channel seismic (MCS) profile. Solid circles are location of ocean bottom seismometers (OBS) O1 – O7. Solid stars mark the locations of the wells Q and H that were drilling during the Joint Industry Project Leg II (JIP II).

Approach

Previously both OBS and MCS data, obtained from USGS, were set up for processing in ProMAX© processing software using the navigation data made available from the field. The MCS data were processed to create a stack. The stacked data were then depth migrated and verified with the well depths. A large-sale (resolution in the order of Fresnel zone) P-wave velocity model using traveltime inversion and a corresponding depth image using pre-stack depth migration (PSDM) were generated through inversion using an approach known as Unified Imaging (UI), which was developed by Jaiswal and Zelt (2008) as a way of testing the Deragowski principle, i.e, the consistency of a velocity model with its corresponding depth migrated image. The velocity profile from traveltime inversion generally captures the background trends but it is not show the details to explain the distribution of gas hydrate and free gas. Hence, the model was refined using Full Waveform Inversion (FWI). We applied frequency-domain full waveform inversion (FWI) (Pratt, 1999) to the 7 OBS data (Fig. 1) in order to obtain a quantitative, high-resolution P-wave velocity model and the attenuation model. At this stage we are interpreting the depth image and the FWI model together.

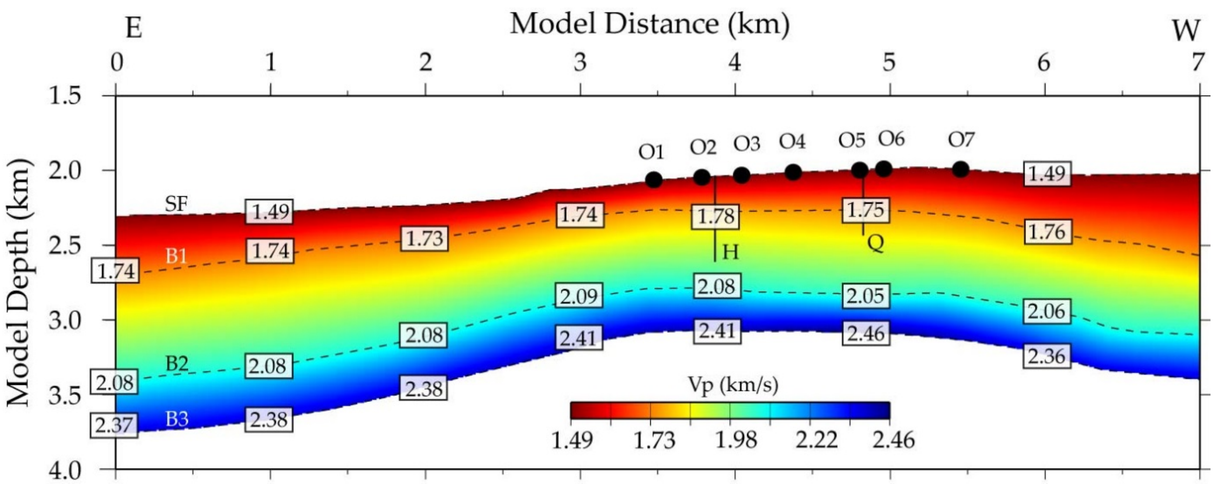

Figure 2. The final V_P model from joint traveltime inversion of OBS and MCS data. OBS, well locations and the magnitude V_P at their respective locations are labeled. Horizons SF – B3 are illustrated with dashed lines.

Traveltime V_P model and the depth image

The velocity-depth model is constructed in a layer-stripping manner with the widely-used Zelt and Smith (1992) inversion algorithm, hereafter referred to as ZS92, which incorporates a Runge-Kutta method for ray tracing and a damped least-square method for computing model updates. The following is a brief introduction of the algorithm, and the reader is directed to the original publication for details. In the ZS92 method, a model is parameterized by the user in discrete layers defined by boundary and velocity nodes that are specified along each layer boundary. An irregular arrangement of trapezoids, with corners corresponding with the user-defined nodes, represents the velocity structure for the purposes of ray tracing. The velocity is linearly interpolated within each trapezoid. Rays are traced through the velocity model in an iterative search mode using zero-order asymptotic ray theory. To linearize the traveltime inversion problem, the algorithm first determines the ray paths in an initial velocity model and then updates the velocity model assuming stationary rays. The data misfit in traveltime inversion is assessed using the normalized form of a misfit parameter referred to as the chi-squared (χ^2) error (Scales *et. al*., 1990):

$$\chi^2 = \frac{1}{n}\sum_{i=1}^{n}\left(\frac{\Delta t_i}{u_i}\right)^2 \qquad (1)$$

In Equation 1, Δt_i is the difference between the predicted and the picked traveltime, n is the number of traveltime picks and u_i is the uncertainty associated with the i^{th} traveltime pick. A χ^2 value of unity indicates that the observed traveltimes have been fitted at their uncertainty levels and that the inverse problem has converged to an acceptable solution (the final model).

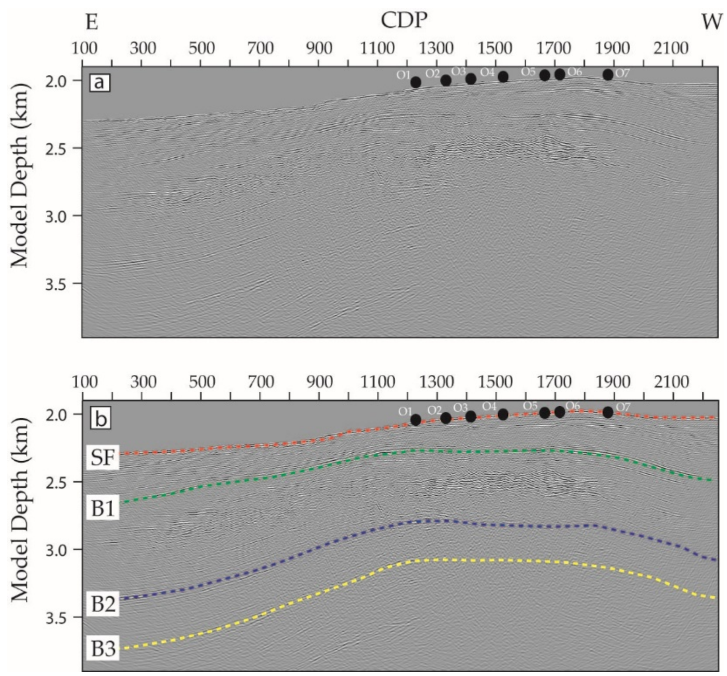

Figure 3. Depth migrated MCS stack (a) un-interpreted and (b) interpreted. The color code in is same as in Figure 3. Migration in (a) and (b) used V_P model from Figure 2. The interpretation in (b) is not manual, the overlaid horizons SF – B3 are estimated from traveltime inversion. The overlay clearly shows a good consistency between migrated and the inverted horizons, strongly validating the kinematic fidelity of migration V_P model.

Full-waveform model

The traveltime model prepared above was improved using a FWI algorithm after *Pratt* [1999]. Pratt's algorithm operates in the frequency domain, where the forward modeling incorporates a visco-acoustic approximation to the elastic wave equation and the inverse problem iteratively updates a starting model to reduce mismatch between the predicted and observed wavefield. Although FWI can also be applied in time domain [*Operto et al.*, 2004], the choice of frequency domain in this paper is driven by (a) efficiency in forward modelling [*Marfurt*, 1984], and (b) the possibility of a multiscale implementation [*Sirgue and Pratt*, 2004]which mitigates the non-linearity of the inverse problem [*Bunks et al.*, 1995].

A brief overview of the method is provided here and the reader is guided to the original paper [*Pratt*, 1999] for detail. In the forward problem, the wavefield is computed by solving the wave equation directly in the frequency domain using the highly accurate, mixed-grid finite-difference approach [*Jo et al.*, 1996; *Štekl and Pratt*, 1998]. In this method, for a model defined on a regular finite-difference grid, absorbing boundary conditions can be implemented at the edges of the model using 45- degree one-way propagators [*Clayton and Engquist*, 1977]. For an individual angular frequency, ω, the wave equation is expressed as:

Error! Bookmark not defined. $\mathbf{d}_{\mathbf{pre}}(\omega) = \mathbf{S}^{-1}(\omega)\mathbf{f}(\omega)$ (2)

In equation (2), $\mathbf{d}_{\mathbf{pre}}$ is the complex-valued predicted wavefield vector from the model vector **m**, **S** is a complex valued impedance matrix that contains information about the physical properties of **m**, and **f** is the source term vector.

The inverse problem minimizes the L_2 norm of the data errors, $\delta\mathbf{d}$, expressed in an objective function, ***E***.

$$\boldsymbol{E}(\mathbf{m}) = \frac{1}{2}\delta\mathbf{d}^{t}\delta\mathbf{d}^{*} \quad (3)$$

In equation (3) **d** is a vector comprising Fourier coefficients of the time-domain data and $\delta\mathbf{d} = \mathbf{d}_{\mathbf{pre}} - \mathbf{d}_{\mathbf{obs}}$, where $\mathbf{d}_{\mathbf{obs}}$ is the observed wavefield, superscript *t* represents matrix transpose, and the superscript * represents the complex conjugate. The Taylor series expansion of $\delta E(\mathbf{m})/\delta\mathbf{m}$ and its simplification in the neighborhood of **m** leads to the following relationship in the k^{th} iteration between the starting, $\mathbf{m}^k$, and the updated, $\mathbf{m}^{k+1}$, model:

$$\mathbf{m}^{k+1} = \mathbf{m}^k - \alpha^k \nabla E^k(\mathbf{m}) \quad (4)$$

In equation (4), $\nabla E(\mathbf{m})$ is the gradient direction and α is the step length (a scalar to replace the Hessian) that is determined by a line search method. The key in the *Pratt* [1999]method is to express the gradient direction as:

$$\nabla E(\mathbf{m}) = \frac{\partial E}{\partial \mathbf{m}} = Real\,\{\mathbf{F}^t[\mathbf{S}^{-1}]^t\delta\mathbf{d}^*\} \quad (5)$$

In equation (5), **F** is known as a virtual source which can be understood as the interaction of the observed wavefield, $\mathbf{d}_{\mathbf{obs}}$, with the perturbations in the model, **m**. Individual elements of the virtual source are defined as $\mathbf{f}^{\,i} = -\frac{\partial \mathbf{S}}{\partial \mathbf{m}_i}\mathbf{d}_{\mathbf{obs}}$, where $\mathbf{f}^{\,i}$ and $\mathbf{m}_i$ are the i^{th} virtual source and model parameters, respectively. Equation (5) is the mathematical expression of the back-propagated residual wavefield, $[\mathbf{S}^{-1}]\delta\mathbf{d}$, being correlated with the forward propagated wavefield, ***F***. The computational complexity in waveform inversion mainly rests on the computation of $\boldsymbol{S}^{-1}$. For multiple source problems, $\mathbf{S}^{-1}$ is best solved using LU decomposition [*Press et al.*, 1992] and ordering schemes such as nested dissection that take advantage of the sparse nature of ***S*** [*George and Liu*, 1981].

Attenuation in the *Pratt* [1999] method is assumed to be a result of absorption, which is a function of the material properties (such as grain size, mineralogy and fluid saturation) and the seisimic frequency. Attenuation is included in the inversion by specifying the velocity model (**m**) as a complex quantity ($\mathbf{m} = \mathbf{m}_r + i\mathbf{m}_i$), where the imaginary ($\mathbf{m}_i$) and the real ($\mathbf{m}_r$) parts are related through the seismic quality factor **Q** as:

$$m_i = -\frac{m_r}{2Q} \quad (6)$$

The *Pratt* [1999] method requires an initial estimate of the seismic source. This estimate, which is input as a function, is updated along with the V_P and Q_P^{-1} models. The waveform inversion begins not only with starting V_P and/or Q_P^{-1} models, but also a starting source signature. For a given data bandwidth, the V_P and Q_P^{-1} models are updated using the current source signature, following which the source signature is updated using the current models. As FWI iteratively incorporates higher wavenumbers, higher frequencies are incorporated in the source signature and the resolution of the recovered model is enhanced. FWI also requires an estimation of density. In this paper, density is modeled as a depth-dependent variable derived using well logs from wells GC955 H and Q.

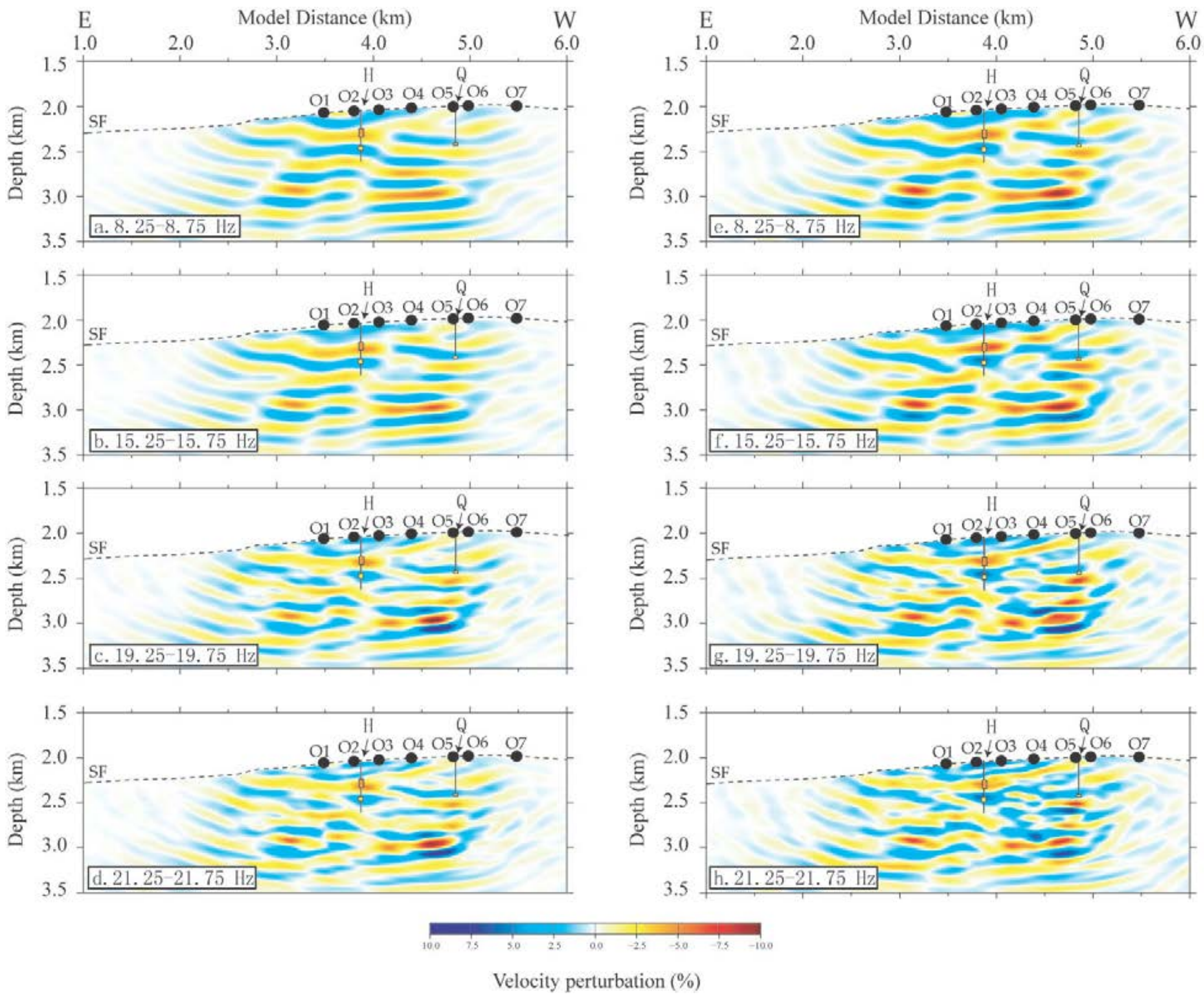

Figure 5. FWI V_P updates. Starting V_P model is shown in Figure 2. Perturbations from first round of inversion a) 8.25 – 8.75 Hz; b) 15.25 – 15.75 Hz; c) 19.25 – 19.75 Hz, and d) 21.25 – 21.75 Hz. e) – h) are from the second round of inversion using the model shown in (b) as the starting model. Other symbols have same meaning as in Figure 3. The orange and yellow markers along H and Q indicate hydrate bearing fine- and coarse-grained reservoirs respectively.

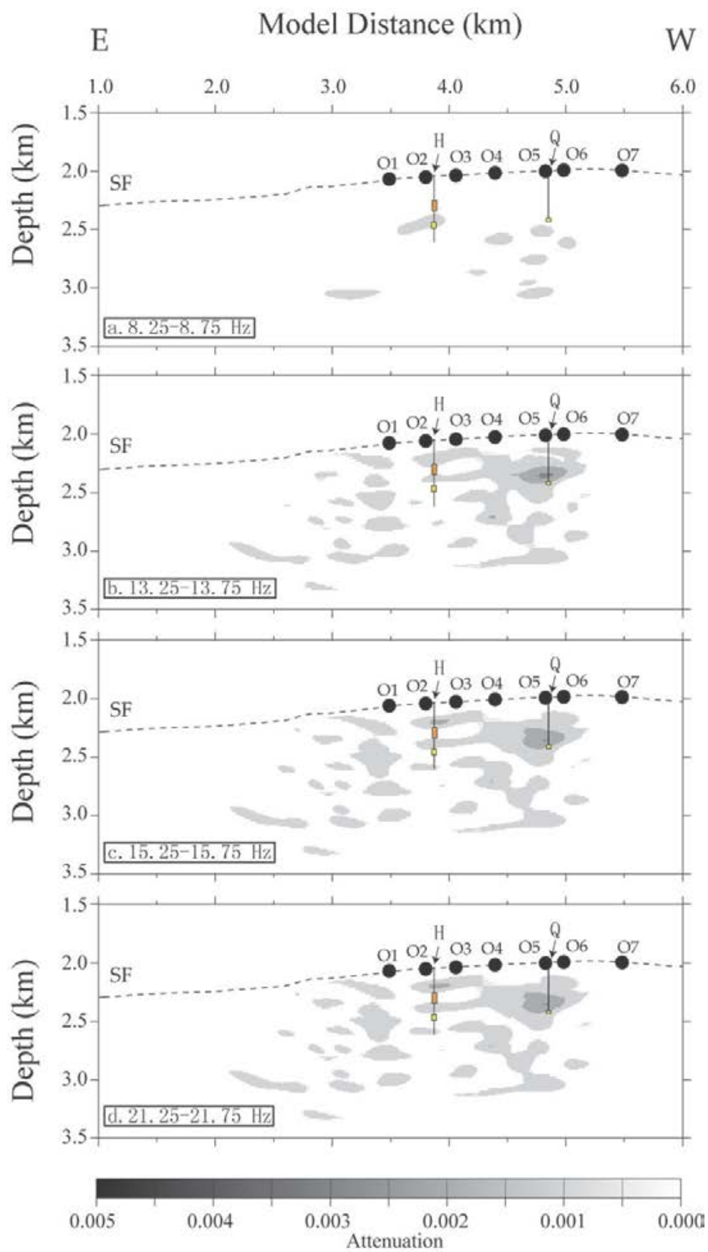

Figure 6. FWI attenuation (Q_P^{-1}) updates. From inversion for a) 8.25 – 8.75 Hz; b) 15.25 – 15.75 Hz; c) 19.25 – 19.75 Hz, and d) 21.25 – 21.75 Hz using a zero starting Q_P^{-1} model and Figure 5h as the starting V_P model. Symbols and colors have the same meaning as in Figure 5. The hydrate-bearing sediments appear to be non-attenuative.

Results:

Traveltime V_P model and depth image

The final V_P model (Figure 2a) is vertically smooth and a continuous function with no velocity jumps across the layer boundaries. Smoothness is desirable when the velocity model needs to be used for depth migration to avoid ringing at the layer interfaces. The first velocity layer is bounded by the seafloor and the horizon B1. Both the seafloor and B1 have anticlinal structures and although these structures are not entirely synchronous (Figures 3) we suggest that the shape is related to the prevailing anticlinal structure in the area that is due to upwelling of the underlying salt. The thickness of the first layer decreases from the edges (0.3 km and 0.375 km respectively at 1.0 km and 6.0 km model distances) towards the center of the model (0.2 km at model distance 3.0km; Figure 7). Structurally, interface B1 it is highest near the Well H location (model distance ~3.75km), it has a strong reflectivity and is easily interpretable throughout the model except between OBSs O3 and O5 (Figure 3) where it is relatively weak. Between O3 and O4, horizon B1 is moderately disrupted showing minor “smiles” which are indicative of diffractions (probably from fault edges) that did not get collapsed during migration (Figure 3). This is expected due to the low resolution of the traveltime V_P model.

The V_P values at top of the first layer are that of the ocean water itself (1.49 km/s). At the base of the first layer, V_P increases laterally from the thicker, eastern (1.74 km/s) and western (1.76 km/s) ends towards the thinner, central part of the model (Figure 2). The V_P gradient within this layer is highest at model location 3.0 km (1.25 km/s/km; Table1). Overall, the increase in the V_P gradient (~50% from flanks to center) is proportional to the layer thickness (~50% from the flanks to crest), suggesting that V_P is may not be completely compaction driven; regardless of the layer thickness the velocities at the base are consistent. Overall, the geometrical structure of B1 from inversion matches very well with its migrated counterpart (Figure 3b).

The second velocity layer is bounded by interfaces B1 and B2. This layer contains the high reflectivity stratigraphy where hydrate-bearing sand dominated sediments were interpreted in wells H and Q and a gas-bearing zone was inferred at the base of the well Q (Figure 3b). Much like B1, the horizon B2 can be identified has a high amplitude continuous reflector from model distances 0 – 3.5 km (CDPs 100 – 1200). Within this interval, the inverted structure of B2 matches well with its migrated counterpart. From 3.5km – 6km model distance (CDPs 1200 – 2000) reflectivity along this horizon is limited. The inverted B2 structure in this interval also has a reasonable coincidence with its migrated counterpart. At model positions west of 6.0 km the agreement between the structures of B2 from inversion increasingly diverges from the migrated reflectivity structure. The second layer has the densest ray coverage between model distance 3.0 km and 5.5 km (CDPs 1000 – 2000). As a result, the velocity model is better constrained in this zone and consequently the migrated structure of high reflectivity package is also most reliable. We have therefore limited our stratigraphic interpretation to positions between CDPs 1000 and 2000 (see below).

Much like B1, horizon B2 has an anticlinal shape. Structurally it is closest to the seafloor at model distance 3.6 km (~CDP 1250). The thickness of the second layer decreases laterally by ~30%, from a maximum of 0.75 km at model distance 1.0 km to a minimum of 0.54 km near Well H location. The V_P gradient is lowest at model distance 1.0 km (0.45 km/s/km) and highest at model distance 3.0 km (0.61 km/s/km). Within this layer, the V_P gradient at Well H (0.55 km/s/km) is higher than at Well Q (0.52 km/s/km). At the base of the second layer, the lowest V_P value is at the location of Well Q; this area of low velocity is most likely related to free gas at the base of Well Q.

The third layer is bounded by interfaces B2 and B3, and its thickness is fairly consistent across the model. The velocity gradient, however, changes by about 100%, from 0.8 km/s/km at model distance 1.0 to 1.64 km/s/km below Well Q. Relative to nearby Vp gradients (1.13 km/s/km at well H and 1.03 km/s/km at model position 6.0 km) the high gradient below well Q represents an abrupt lateral change. This is presumably related to the low velocity at the top of the third layer at well Q, associated with the free gas. But it is noteworthy that the depth image, does not show any unusual reflectivity patterns, and thus sheds little light on this subsurface heterogeneity.

Full waveform model

Model updates from FWI were subtle, with the total change from the starting to the final model being less than ±10% of the model velocity. As a result, it is more reasonable to examine the V_P perturbations for their geological sensibility than the V_P model as a whole. Perturbation models for both rounds of the FWI are shown in Figure 4 and is calculated as $(V_P^{final}–V_P^{start})/ V_P^{start}$. Perturbation is considered positive if V_P increases with respect to the starting model, i.e, $[(V_P^{final}–V_P^{start})/ V_P^{start}] > 0$. In general the polarity of the perturbations (positive or negative) were fairly consistent between the two rounds of FWI (i.e, if lower frequencies perturb the starting velocities in one direction at a particular spatial location, higher frequencies augment this adjustment). The magnitude of perturbation were larger and the perturbation features were better defined at the end of the second round of Vp inversion than at the end of the first round. Comparison with borehole and seismic data provides a means for assessing the validity of FWI results. In the well H log, high velocities are present within the interval from ~2.45-2.50 km model depth and the FWI results appear to show a corresponding high Vp perturbation at this at this model location. Further, a negative perturbation is present in the FWI results immediately below the bottom of Well Q in the location where free gas was inferred, providing further qualitative validation of the FWI V_P model.

The area of hydrate in fine-grained sediments in Well H (at depths of approximately 2.25 to 2.35 km) is associated with a negative velocity perturbation (Figures 4) but this does not imply a discrepancy between the FWI results and the borehole data. Rather, this perturbation is a necessary refinement to the smooth starting model. In the coupled inversion-migration approach, which provided the starting model for FWI, this area was parameterized as part of a thick layer that included both the fracture-filling hydrate and the deeper sand-hosted gas hydrate accumulations. As a result, velocities were averaged over a large spatial zone and the high velocity of the sand-hosted gas hydrate was “smeared” across the full layer. We suggest that the negative velocity perturbation in the area of hydrate in fine-grained sediment is simply a refinement, or correction, for this area of the model where velocity was originally over-predicted due to the parameterization of the inversion/migration model.

More detailed assessment of the FWI V_P model is done at well H and G locations through comparison with their respective sonic logs (Figure 7). Well logs have higher spatial resolution (greater wavenumber content) than the V_P model that has been constructed using surface seismic. To make the comparison internally consistent, the sonic logs were decomposed and then reconstructed using the range of wavenumbers that were imaged in the FWI. Thus, in Figure 7, attention should be paid to the relation among the starting (red line) and final (green line) FWI V_P models and the reconstructed H and Q logs (plotted as yellow lines). As expected, the FWI velocities have a better agreement with the reconstructed sonic logs than with the original logs. In terms of general trends, the improvement from initial to final model is clearly evident and the agreement between the final model and the reconstructed sonic log is reasonable in both the hydrate-bearing fine- and coarse-grained reservoirs. In particular, at the interval of sand-hosted gas hydrate in Well H, the FWI V_P is greater than 2.0 km/s and in the area of inferred free gas below the bottom of Well Q, the FWI V_P decreases to 1.6 km/s.

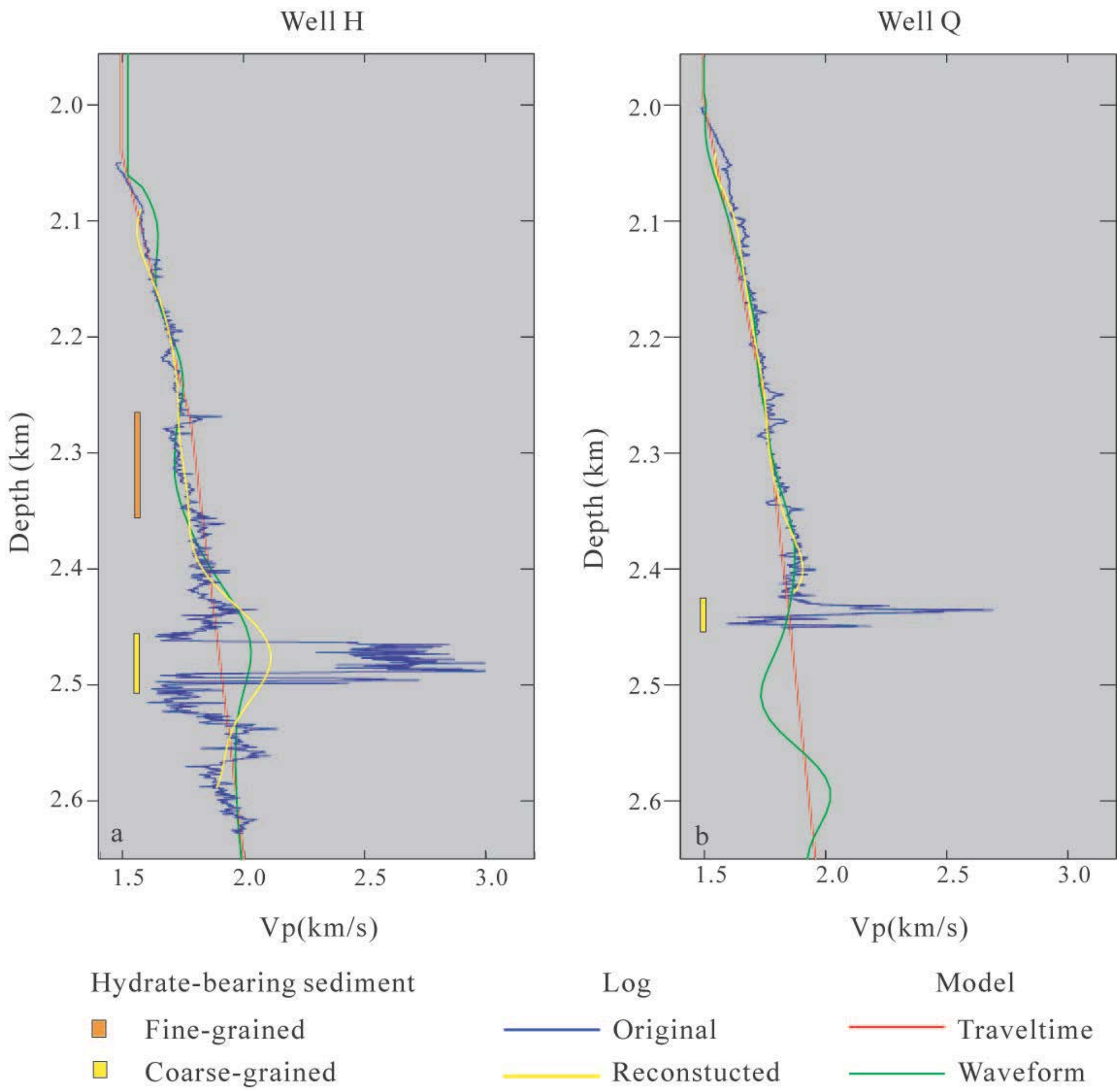

Figure 6. FWI V_P comparison with sonic logs from a) Well H and (b) Well Q. In (a) and (b) the color codes are as follows: blue is the sonic log, yellow is the filtered log (see text for details), red is the V_P from the starting model (Figure 3), and green is the V_P from the final FWI model (Figure 4h).

The V_P model from the second round of inversions, and the corresponding source signature, were used for estimating Q_P^{-1} updates. The initial Q_P^{-1} model assumed zero attenuation. Inversion of the lowest frequency group, 8.25-8.75 Hz, yields the first set of Q_P^{-1} updates, which were fairly smooth in character (Figure 6a). Successive inversion of higher frequencies groups resolved the finer-scale attenuation structure (Figures 6). For consistency, the frequency groups were kept same as in the V_P inversion. Both the source and the V_P were allowed to change simultaneously, along with Q_P^{-1}, in each step of Q_P^{-1} inversion. However, the V_P and source updates were minimal, likely due to the higher sensitivity of amplitudes towards Q_P^{-1} [*Jaiswal et al.*, 2012]. Much like in the V_P inversion, frequencies over 21.75 Hz yielded excessively noisy results. Much like their V_P counterpart a second round of Q_P^{-1} inversion was also attempted, but improvements in results were achieved. As a result, Q_P^{-1} model from 21.25 – 21.75 Hz inversion was considered final.

Composite Interpretation

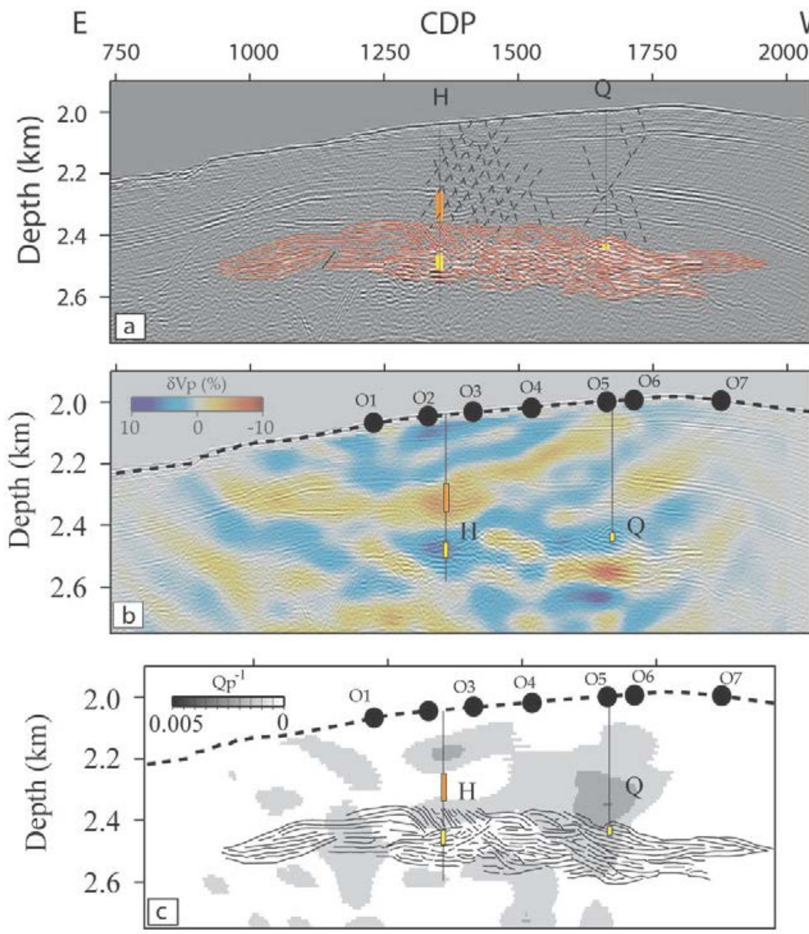

Figure 8. Composite Interpretation. (a) Structural interpretation. The faults appear to have two major orientation. The hydrate bearing zones at both the wells are color coded. Line drawings of the high reflectivity zone between horizons B1 and B2, which is interpreted as channel stratigraphy. Also, faults stemming from the channel system are interpreted. (b) Overlay of the final depth image and final V_P perturbations. (d) Overlay of the interpreted channel system on the final attenuation model.

In the depth migrated profile, morphology of a channel/levee complex can be interpreted in a way that suggests Well H lies along the channel axis and Well Q is within the levee (Figure 8a). An overlay of the depth image and the final perturbation model (Figure 8b) does not show any clear correspondence between the V_P perturbation trends and the interpreted stratigraphy. The velocity perturbations are more heterogeneous within the channel/levee body than above or below it, which probably indicates compartmentalization and heterogeneous distribution of gas, gas hydrate and water. This compartmentalization may be controlled by faulting and/or by grain size and sorting, as discussed by [*Boswell et al.*, 2012a].

In the absence of the sonic logs, it is difficult to definitively link V_P perturbations with hydrate or free gas. The sonic log in well H suggested that V_P within the hydrate-bearing coarse-grained sediments is at least 20% greater than the background velocity. The FWI modeling, however, shows a more modest velocity, ~10% greater than the background, likely due to the fact that the FWI model corresponds with velocities averaged over a larger volume of sediments than the logs. The velocity anomaly observed in the FWI results would likely have more closely matched the well logs if the hydrate-bearing sands were spatially (both vertically and laterally) more extensive. An additional complication to interpretation was mentioned in the previous section; a negative velocity perturbation may represent a refinement to a velocity that was originally over-predicted, rather than a velocity that is low in an absolute sense. Thus for the case of the depth range of 2.25 and 2.35 km at Well H, a negative FWI velocity perturbation corresponds spatially with low saturations of gas hydrate within fractures of fine-grained sediment [*Boswell et al.*, 2012b].

Within the channel-levee complex, the maximum positive velocity perturbation in the FWI model is at the location where Well H encountered gas hydrate in the coarse-grained sediments (Figure 10c). Likewise the largest velocity decrease in the FWI model is at the base of Well Q (Figure 8c), where free gas has been inferred to exist. Away from the wells H and Q, within the resolution of the FWI results, only a modest presence of hydrate or free gas can be speculated. In addition, interpretations away from the boreholes must consider the possibility that velocity perturbations could be indicative of lithological changes rather than hydrate and free gas variation.

An overlay of the Paper 1 channel/levee interpretation on the attenuation model (Figure 8c) shows that the two known hydrate-bearing zones sampled by Well H have subdued attenuation relative to the background sediment. Attenuation is most significant in the vicinity of well Q but we note that attenuation is not as high beneath Well Q, where free gas was inferred, as it is along the wellbore immediately above the gas pocket (Figure 8c). *White* [1975] argued that attenuation and gas saturation may not have a linear relation; that for low gas saturations attenuation increases with increasing gas saturation and that above a certain saturation threshold attenuation decreases with increasing saturation. Based on this interpretation, the high attenuation near Well Q raises the possibility of the presence of free gas (probably in the bubble phase) within the upper 400m below the seafloor. As attenuation is more sensitive than velocity to pore fluid content [*White*, 1975], this interpretation suggests the any gas would be present in low enough saturation to impact the attenuation but not the velocity. Borehole data, however, do not suggest the presence of free gas in the upper 400 m of Well Q, and seismic data show greater evidence for vertical fluid migration pathways near Well H than well Q [*Haines et al.*, 2014].

No geothermal gradient were measured in wells H and Q. Collett et al. (2012) used 32^0C/km for computing fluid resistivity. Although this value of gradient puts the BHSZ close to the base of well Q, it is somewhat higher than the regional average proposed by other researchers such as [*Jones et al.*, 2003]. Using the seafloor depth-temperature relation suggested by [*Milkov and Sassen*, 2001], the BHSZ is predicted for a range of geothermal gradients from 23^0C/km – 32^0C/km and overlaid on the FWI perturbation model (Figure 8a). The BHSZ predicted using the gradient value used by [*Collett et al.*, 2012], 32^0C/km, appears to be a fairly good representative of the BHSZ (Figure 8a). It connects the inferred hydrate-gas interface in the area of Well Q to a stratigraphic level immediately below established hydrate-bearing sand reservoirs in Well H. East of Well H, between CDPs 1000 and 1250, the BHSZ predicted with this gradient appears to follow a positive-to-negative (blue-to-yellow) V_P perturbation phase change, which could be the eastward extension of the BHSZ. If indeed so, it is notable that the seismic expression of BHSZ in this case is neither in the reflectivity stack (Figure 8b) nor in the “whole” velocity model, but in the perturbation model.

Conclusions:

A V_P model and depth image of shallow stratigraphy in GC955 was obtained in this paper by coupling traveltime inversion with depth migration using high-resolution MCS data and OBS data. The coupling was based on seeking a common structural solution for three horizons. The resulting depth image enables interpretation of a compartmentalized channel-levee system. The V_p and $Q^{-1}{}_p$ models were estimated from frequency-domain FWI of seven OBS gathers. Data preconditioning and starting model choice were essential for FWI to converge to a reasonable geological model. The minimum and the maximum frequencies used in the inversion were 8.25 and 21.75 Hz respectively. Halting criteria included geological sensibility of the evolving V_P and Q_P^{-1} perturbations, real and simulated data similarity, and objective function convergence. FWI provided physical properties information complementary to the pre-stack migrated depth image.

It is possible that Well GC955-H, which encountered high hydrate saturation penetrated the coarse-grained axial zone and Well GC955-Q penetrated the levee of this channel complex. Imaging shows strong evidence that a) the channel-levee system has a complex and compartmentalized architecture; and b) the hydrate in the coarse and fine-grained sediments at GC955 site are closely linked though faults. A composite map of reflectivity and FWI V_P agrees with other indications that the sand-dominated channel/levee body is internally compartmentalized and that both hydrate and free gas have patchy distributions. Hydrated sediments appear to be seismically non-attenuative in this area. The top of the free gas pocket at Well Q, the base of the hydrate-bearing coarse-grained sediments in Well H, and perturbation structures are most consistent with a BSHZ that corresponds with a geothermal gradient of 32^0C/km. These results further illustrate the value of FWI for characterizing gas hydrate accumulations; LWD data at GC955 provide valuable corroboration for the FWI results, validating the methodology and lending confidence to cases where FWI may be applied at sites lacking borehole data.

Milestone Status:

Milestone	Description	Status	Schedule
Traveltime Inversion Model	The recipient shall compare the real and predicted reflection traveltimes from the final velocity model to be used for PSDM.	Done for CGGVeritas Datase and for the USGS dataset	Completed on target
Depth Migrated Image	The recipient shall compare structure and stratigraphy between the final depth image and images in literature and SSRs.	Done	Completed on target
Waveform velocity model	The recipient shall compare waveform inversion velocity and sonic logs at well locations.	Done	Completed On target
Waveform attenuation model	The recipient shall compare real and synthetic simulated data.	Done	Completed On target
Rock physics model	The recipient shall compare predicted hydrate saturation at well locations with that available in the literature and methods of other DOE funded PIs, if available.	Ongoing	On target
Saturation map	The recipient shall compare consistency between hydrate distribution and structural/stratigraphic features interpreted in the study area.	Ongoing	On target

References:

Boswell, R., M. Frye, D. Shelander, W. Shedd, D. R. McConnell, and A. Cook (2012a), Architecture of gas-hydrate-bearing sands from Walker Ridge 313, Green Canyon 955, and Alaminos Canyon 21: Northern deepwater Gulf of Mexico, *Marine and Petroleum Geology*(0).

Boswell, R., T. S. Collett, M. Frye, W. Shedd, D. R. McConnell, and D. Shelander (2012b), Subsurface gas hydrates in the northern Gulf of Mexico, *Marine and Petroleum Geology*(0).

Bunks, C., F. M. Saleck, S. Zaleski, and G. Chavent (1995), Multiscale seismic waveform inversion, *Geophysics*, *60*(5), 1457-1473.

Clayton, R., and B. Engquist (1977), Absorbing Boundary-Conditions for Acoustic and Elastic Wave-Equations, *Bulletin of the Seismological Society of America*, *67*(6), 1529-1540.

Collett, T. S., M. W. Lee, M. V. Zyrianova, S. A. Mrozewski, G. Guerin, A. E. Cook, and D. S. Goldberg (2012), Gulf of Mexico Gas Hydrate Joint Industry Project Leg II logging-while-drilling data acquisition and analysis, *Marine and Petroleum Geology*(0).

George, A., and J. Liu (1981), *Computer Solution of Large Sparse Positive Definite Systems*, Prentice Hall, Englewood Cliffs, NJ.

Haines, S. S., P. E. Hart, C. D. Ruppel, T. O'Brien, B. Wayne, J. White, E. Moore, P. D. Ferro, and P. Lemmond (2014), Cruise report for P1-13-LA, U.S. Geological Survey gas hydrates research cruise, R/V Pelican April 18 to May 3, 2013, deepwater Gulf of Mexico,*Rep.*, 33 pp, U.S. Geological Survey.

Jo, C. H., C. Shin, and J. H. Suh (1996), An optimal 9‐point, finite‐difference, frequency‐space, 2-D scalar wave extrapolator, *Geophysics*, *61*(2), 529-537.

Jones, G. D., P. J. Barton, and S. C. Singh (2003), Combined structure and velocity stacks via the tau-p transform, *Geophysical Prospecting*, *51*(3), 205-213.

Marfurt, K. J. (1984), ACCURACY OF FINITE-DIFFERENCE AND FINITE-ELEMENT MODELING OF THE SCALAR AND ELASTIC WAVE-EQUATIONS, *Geophysics*, *49*(5), 533-549.

Milkov, A. V., and R. Sassen (2001), Estimate of gas hydrate resource, northwestern Gulf of Mexico continental slope, *Marine Geology*, *179*(1-2), 71-83.

Operto, S., C. Ravaut, L. Improta, J. Virieux, A. Herrero, and P. Dell'Aversana (2004), Quantitative imaging of complex structures from dense wide-aperture seismic data by multiscale traveltime and waveform inversions: a case study, *Geophysical Prospecting*, *52*(6), 625-651.

Pratt, R. G. (1999), Seismic waveform inversion in the frequency domain, Part 1: Theory and verification in a physical scale model, *Geophysics*, *64*(3), 888-901.

Press, W. H., S. A. Teukolsky, W. T. Vetterling , and B. P. Flannery (1992), *Numerical Recipes in C : the art of scientific computing*, 2nd ed., University Press.

Sirgue, L., and R. G. Pratt (2004), Efficient waveform inversion and imaging: A strategy for selecting temporal frequencies, *Geophysics*, *69*(1), 231-248.

Štekl, I., and R. G. Pratt (1998), Accurate viscoelastic modeling by frequency‐domain finite differences using rotated operators, *Geophysics*, *63*(5), 1779-1794.

White, J. (1975), COMPUTED SEISMIC SPEEDS AND ATTENUATION IN ROCKS WITH PARTIAL GAS SATURATION, *GEOPHYSICS*, *40*(2), 224-232.

National Energy Technology Laboratory

626 Cochrans Mill Road

P.O. Box 10940

Pittsburgh, PA 15236-0940

3610 Collins Ferry Road

P.O. Box 880

Morgantown, WV 26507-0880

13131 Dairy Ashford Road, Suite 225

Sugar Land, TX 77478

1450 Queen Avenue SW
Albany, OR 97321-2198

Arctic Energy Office

420 L Street, Suite 305

Anchorage, AK 99501

Visit the NETL website at:

www.netl.doe.gov

Customer Service Line: 1-800-553-7681